Ice flow velocity of the Nioghalvfjerdsfjorden Glacier and Zachariæ Isstrøm, Northeast Greenland, in the 1960s from Historical Satellite Imagery

Litao Dai [1,2], Xingchen Liu [1,2], Lu An [1,2], Rongxing Li [1,2]

[1] Center for Spatial Information Science and Sustainable Development Applications, Tongji University, 1239 Siping Road, Shanghai, China - (2233699; xcliu; anlu2021; rli)@tongji.edu.cn
[2] College of Surveying and Geo-Informatics, Tongji University, 1239 Siping Road, Shanghai, China

Keywords: Northeast Greenland, Ice flow velocity, Ice motion, Glacier

Abstract

The Northeast Greenland Ice Stream (NEGIS) is experiencing sustained accelerated mass loss due to the combined effects of atmospheric and ocean warming. The Nioghalvfjerdsfjorden glacier (NG) and Zachariae Isstrøm (ZI) are major contributors to the mass balance in NEGIS, draining 12% of the Greenland Ice Sheet (GrIS). Precise measurements of the ice flow velocities of NG and ZI are crucial for estimating the mass balance in NEGIS and predicting future sea level rise. However, the study of early NEGIS is limited by the lack of ice flow velocity before 1985. We proposed a systematic process for orthorectification on CORONA KH-4A imagery, which proved to be efficient and accurate, yielding 25 m precision. Using a hierarchical network densification approach based on ARGON KH-5 and CORONA KH-4A imagery, we successfully generated the ice flow velocity map for NG and ZI from 1963 to 1967. The results showed different changes in ice flow velocity over a 57-year period for NG and ZI. The average ice flow velocity near the grounding line increased by 12.4% for NG and 81.4% for ZI from 1963 to 2020. This paper filled a gap in historical ice flow velocity data for NEGIS and provided early, and valuable information for studying the long-term motion of ice flow. It can also improve the prediction accuracy of future changes in mass balance in this region.

1. Introduction

Mass loss from the Greenland Ice Sheet (GrIS), the second largest ice sheet on Earth, has been the most significant contributor to sea level rise in recent years. The loss is primarily attributed to the ongoing dynamics of outlet glaciers (King et al., 2020). It has been found that the Northeast Greenland Ice Stream (NEGIS) is experiencing sustained accelerated mass loss due to the combined effects of atmospheric and ocean warming (Rignot et al., 2017). Nioghalvfjerdsfjorden glacier (NG) and Zachariae Isstrøm (ZI) are the major contributors to the mass balance in NEGIS, which together hold enough ice to raise global sea level by 0.57 m and 0.54 m, respectively (An et al., 2021).

The NG is currently Greenland’s largest ice tongue and drains approximately 8.4% of the GrIS. The ice shelf is anchored in a 20-km-wide valley, with the part near the grounding line thinned by 30% between 1999 and 2014 (Mayer et al., 2018). The main ice front is divided into five sections by two islands and three ice rises (Reeh et al., 2001). The ZI has begun a rapid retreat since the large loss of the ice shelf in 2003. The ice shelf collapsed between late 2012 and early 2013, reducing its area by 95% and doubling its ice flow velocity (Mouginot et al., 2015). The rapid thinning of NG and the disintegration of ZI have been related to warmer ocean temperatures and increased surface melt (Schaffer et al., 2020; Millan et al., 2023). It has been found that ZI will become extremely unstable in the upcoming decades, while bedrock's stabilizing influence will keep NG relatively stable throughout this century (Choi et al., 2017). The dynamics of NG and ZI highlight the extreme sensitivity and vulnerability of NEGIS to climate change. To assess future mass balance and predict future sea level rise more accurately in NEGIS, a long-term perspective of the ice flow velocities is urgently needed to understand the stability of this region.

The methods for measuring ice flow velocity primarily include ground-based methods and remote sensing monitoring. Early ground-based measurements used observational tools such as snow stakes (Wallerstein, 1958), electronic distance meters, or theodolites (Olesen et al., 1969), which were usually inefficient and costly. Although the development of the Global Positioning System (GPS) has improved the accuracy of ice flow velocity, ground-based measurements are still limited by harsh environmental conditions. With the advancement of remote sensing technology, large-scale and high-precision monitoring of glacier movement has become possible. Radar and optical imagery are the primary data sources for measuring ice flow velocity using remote sensing methods. Radar imagery, mainly obtained after the 1990s, is widely used in ice flow velocity measurement based on offset tracking and interferometry techniques (Moon et al., 2012; Joughin, 2022). Optical remote sensing measures ice flow velocity primarily through image feature tracking and correlation calculation principles (Rosenau et al., 2015; Gardner et al., 2018). The development of automated feature tracking technology has greatly improved the accuracy and efficiency of ice flow velocity measurements. Moreover, optical imagery is lower-cost and provides longer temporal coverage compared to radar imagery, making it an indispensable technological tool for monitoring long-term glacier movement.

Although optical satellite imagery has been available since the 1970s, early applications primarily used to extract glacier ice fronts and continuous optical images for studying glacier flow velocity in northeast Greenland have been scarce. Declassified intelligence satellite photography (DISP) imagery from the 1960s is valuable data for studying historical glacier changes

(Kim et al., 2007), but it has not yet been extensively processed to map ice flow velocity. The military satellite systems code-named CORONA (KH-1 to KH-4B), ARGON (KH-5), and LANYARD (KH-6) acquired photographic images from space and returned the film to Earth for processing and analysis (McDonald, 1995). However, long-term storage of film makes early satellite images more distorted, which makes image processing more difficult compared to recent remote sensing images. Two full-coverage mosaics of Greenland were successfully created using ARGON images by the self-calibration block bundle adjustment model (Zhou et al., 2002). The frame camera system of the ARGON image allows the application of traditional frame-based aerial photogrammetry with only minor modifications (Sohn et al., 2004). Compared to ARGON imagery, CORONA imagery collected by a non-frame dynamic sensor will have more geometric distortions, with the greatest distortions occurring at the edges of the image (Shin, 2003). Furthermore, there is no calibration report or orbit ephemeris data for CORONA imagery, making traditional image orientation methods unsuitable for such imagery. Some studies have proposed several rigorous mathematical models to address distortions in CORONA images with high accuracy (Sohn et al., 2004; Shin et al., 2008). However, there are currently few practical and efficient orthorectification methods or procedures available.

In this paper, we proposed an efficient and systematic process for CORONA KH-4A orthorectification which can be easily replicated. We mapped the ice flow velocity of NG and ZI using ARGON and CORONA imagery based on the methods presented by Li et al. (2017) and Ye et al. (2017) and analyzed the ice flow velocity variations between 1963 and 2020.

2. Data and Methods

2.1 Data

The ARGON satellite has a frame camera with a focal length of 7.62 cm. Each film frame measures approximately 11.43 cm × 11.43 cm, covering an area of about 500 km × 500 km. The ground resolution is approximately 140 m, digitized at 7 μm per pixel by the United States Geological Survey (USGS) Earth Resources Observation and Science Center Scanning Department in the 1990s. This paper selected an image from mission 9058A with minimal cloud coverage for estimating ice flow velocity.

The KH-4A system on the CORONA satellite offers a higher ground resolution of approximately 2.74 m and more distinct textural features compared to the ARGON imagery. It is equipped with a dual panoramic camera system (forward (FWD) and afterward (AFT)), providing about 10% overlap between adjacent strips. The FWD camera points forward 16.5° from nadir and the AFT camera points backward 13.5° from nadir with a convergence angle of 30°. Each camera has a scanning angle of 70° and a single lens with a focal length of 60.96 cm (Shin, 2003). When selecting images, priority should be given to those centered over the study area to avoid stitching along vertical edges (Iacone et al., 2022). All images should be acquired simultaneously and from the same camera direction. The CORONA images selected for this study are all AFT. The coverage of images chosen for mapping ice flow velocity and study area location are shown in Figure 1. Detailed information about the images is provided in Table 1.

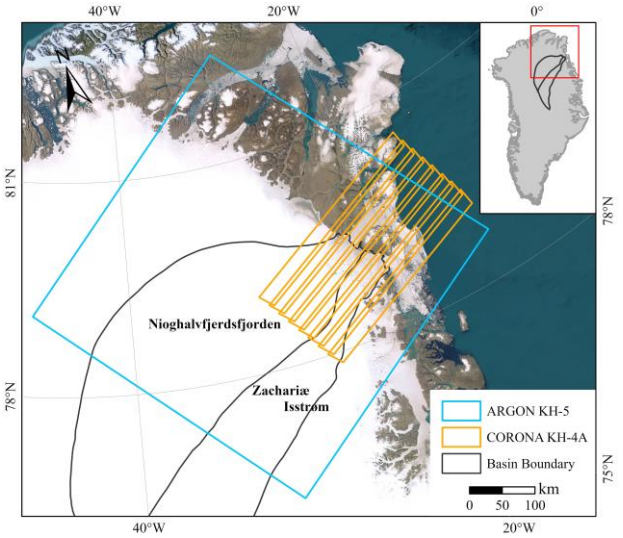

Figure 1. The location of study area with the coverage of DISP images, ESRI World Imagery as the background.

Satellite system	Acquisition date	Image ID	Camera
ARGON	09/01/1963	DS09058A038MC002	A frame camera
CORONA	04/05/1967	DS1040-2090DA006 DS1040-2090DA007 DS1040-2090DA008 DS1040-2090DA009 DS1040-2090DA010 DS1040-2090DA011 DS1040-2090DA012 DS1040-2090DA013	Two panoramic cameras

Table 1. Detailed information of the DISP images in this paper

The 25-m-resolution AERODEM (Korsgaard et al., 2016), 30-m-resolution MEaSUREs Greenland Ice Mapping Project Digital Elevation Model, and 15-m-resolution MEaSUREs Greenland Ice Mapping Project 2000 Image Mosaic (Howat et al., 2014) were used as vertical and horizontal references. In addition, this paper analyzed the long-time motion of ice flow using published ice flow velocity products. The reference data used is summarized in Table 2.

	Products
Horizontal reference	MEaSUREs Greenland Ice Mapping Project 2000 Image Mosaic
Vertical references	MEaSUREs Greenland Ice Mapping Project Digital Elevation Model AERODEM
Ice flow velocity map references	MEaSUREs Greenland Annual Ice Sheet Velocity Mosaics (Joughin, 2022) ITS_LIVE (Gardner et al., 2018)

Table 2. Reference data used in this paper

2.2 Orthorectification of CORONA Images

2.2.1 Preprocessing: A complete CORONA KH-4A strip is scanned by USGS at 7 µm into four separate subfiles, each with a 5% overlap. These four subfiles should first be stitched into a single strip prior to geographic registration. Affine transformation is employed by selecting points with the same features within the overlapping regions to merge the subfiles. Since this involves simply joining the files, grayscale information from the overlapping regions should be derived from one of the parts rather than averaging both parts during mosaicking (Iacone et al., 2022).

The images generate black thin film borders during the scanning process, which should be cropped before orthorectification to retain the valid image area. The center of the cropped strip is approximated as the center of the panoramic image for subsequent panoramic distortion correction calculations.

2.2.2 Panoramic Distortion Correction: Panoramic distortion arises from the cylindrical shape formed by panoramic lenses during scanning. Panoramic distortion correction is to transform the panoramic image coordinates in cylindrical film into the frame image coordinates in a tangential plane. The geometric relationships between panoramic image coordinates and frame image coordinates are as follows (Figure 2):

$$\alpha = (x_a - x_0)\frac{d}{f} \tag{1}$$

$$x_A - x_0 = \frac{f}{d}\tan\alpha \tag{2}$$

$$y_A - y_0 = (y_a - y_0)\sec\alpha \tag{3}$$

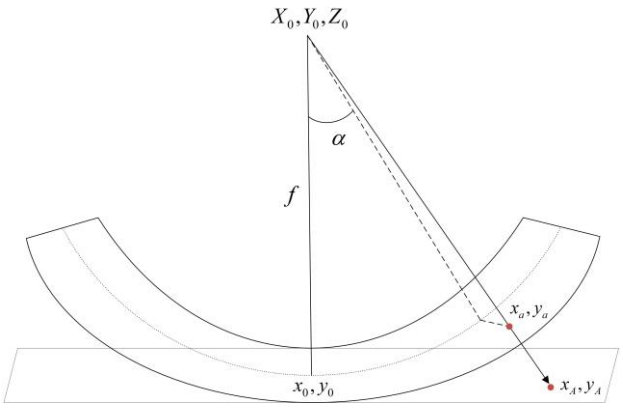

Figure 2. The geometric relationships between panoramic image coordinates and frame image coordinates.

where α = camera scan angle

d = film scan resolution

f = focal length

X_0, Y_0, Z_0 = coordinates of the perspective centre

x_0, y_0 = coordinates of the panoramic film centre

x_a, y_a = panoramic image coordinates in cylindrical film

x_A, y_A = frame image coordinates in a tangential plane

Due to the lack of camera calibration files, the film center coordinates in the above equation cannot be precisely located. This paper approximates the center of the cropped strip after black border removal as the center of the panoramic image.

2.2.3 Bundle Adjustment: Bundle adjustment is the process of establishing mathematical relationships between images, sensor models, and objects on the ground, providing approximate values for the exterior orientation elements of each image and the coordinates of ground points. Bundle adjustment requires a set of control points connecting the image to the ground and tie points connecting the different strips (Kim, 2004).

Control points were selected with reference to Feng’s guidelines on stable features such as bare rock and ice rises (Feng et al., 2023). These features typically have minimal change over long periods. Control points on each strip should be evenly distributed as much as possible, with approximately equal numbers selected on both sides along the long edge, to avoid an imbalance of points between two sides. The selection of the tie points is based on the automatic generation with manual selection supplemented. Adjacent tie points should be distributed on different sides of the overlap region to prevent them from forming a straight line.

2.3 Orthorectification of ARGON Images

The image was captured during the Arctic summer, resulting in overexposure. An adaptive histogram equalization method was employed to enhance the images, improving local contrast and addressing issues where textures were obscured due to exposure. Mean smoothing filtering was applied to reduce noise and minimize speckles in the images.

Image orientation consists of two parts: internal and external orientation (IO and EO). Indistinct or incomplete fiducial points can be identified using a semi-automatic fiducial mark recognition algorithm, which is used to transform from an image coordinate system to a scanner coordinate system using a second-order polynomial transformation. Lens distortion can be corrected using lens distortion parameters and formulas provided in the camera calibration report (Ye et al., 2017). Initial exterior orientation elements can be interpolated from ephemeris files using Lagrange interpolation and refined using bundle adjustment for EO. The guidelines for selecting control points are the same as in the CORONA KH-4A imagery.

2.4 Ice Flow Velocity Measuring

2.4.1 Image Matching: The core of detecting ice flow velocity using early remote sensing data relies on optical image matching techniques. We used a hierarchical matching method of feature points and grid points with additional triangulation constraints proposed by Li et al. (2017). Ice flow texture features on image pairs are visually identified as the first layer of constraints for the triangulation mesh. Subsequently, manually selected points are used to match feature points and grid points, compensating for local areas with poor visual effects. Parameters to be set primarily include the size of the reference window and the search radius. A large reference window can increase mismatches, while a small one may fail to identify effective features and correct matching points. The search radius is determined by the ice displacement between image pairs.

2.4.2 Error Elimination and Adjustment: There are certain mismatches in the matched points (feature and grid points) due to the noise in the image, necessitating further improvement by eliminating the mismatches to enhance matching accuracy. This paper combined both manual and automated methods to eliminate mismatches based on the correlation coefficient of matched points, ice flow velocity values, and direction. The threshold for correlation coefficients is determined from the statistical analysis of manual points. Eliminate points deviating more than three times the standard deviation from the smoothed flow velocities to eliminate mismatched ice flow velocities. Mismatches in flow direction are addressed by applying different angle thresholds in various regions for removal. Using the natural interpolation method on combined manual points, feature points, and grid points to generate the ice flow velocity map, which can supplement and fit the positions of the unmatched points.

Ice flow shows varying acceleration or deceleration during movement from the interior of ice sheets to the ice front, leading to a potential overestimation or underestimation of average speeds calculated through feature tracking and point matching. This paper used the method proposed by Li et al. (2022) to correct for overestimations and underestimations for ice flow velocity adjustments.

2.4.3 Uncertainty: The accuracy of the ice flow velocity map (σ_{vlc}) is evaluated by four components: orthorectification accuracy of the two images (σ_{ortho1} and σ_{ortho2}), accuracy of identifying feature points (σ_{ident}), and accuracy of image matching (σ_{match}). Δt is the time interval between the image pairs. The formula for calculating the ice flow velocity map’s accuracy is as follows:

$$\sigma_{vlc} = \frac{\sqrt{\sigma_{ortho1}^2 + \sigma_{ortho2}^2 + \sigma_{ident}^2 + \sigma_{match}^2}}{\Delta t} \quad (4)$$

3. Result

3.1 Orthorectification of DISP Images

We manually measured the image coordinates of the control points on CORONA KH-4A imagery and their geodetic coordinates in the reference system (WGS 1984 NSIDC Sea Ice Polar Stereographic North) based on horizontal and vertical references. This paper used ERDAS software for the bundle adjustment process, with a total of 157 control points and 116 tie points on eight strips. The orthorectification accuracy was calculated to be around 25 m by selecting check points on the reference image. The distribution of three types of points is shown in Figure 3.

The internal orientation error of the ARGON image was 0.32 pixels in ERDAS. The total number of 54 control points was selected in the bundle adjustment process, and the orthorectification accuracy by selecting check points is approximately 53 m.

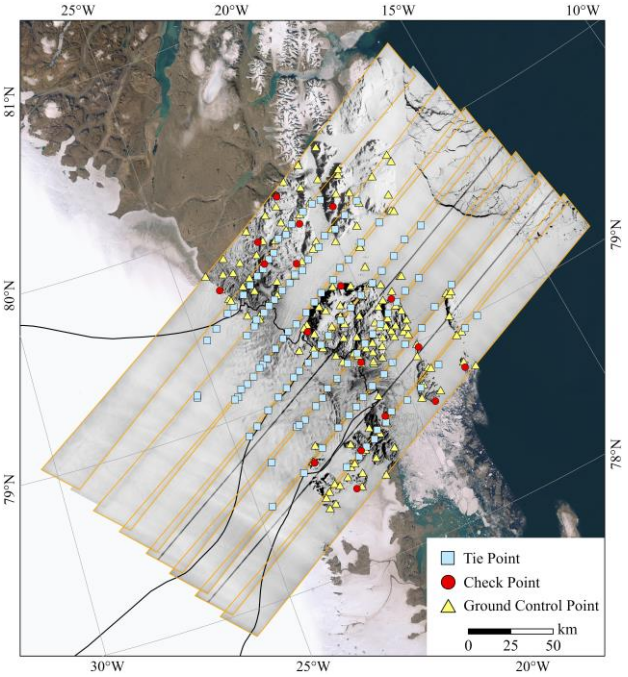

Figure 3. Distribution of tie points (blue square), check points (red circle), and ground control points (yellow triangle) overlayed on CORONA KH-4A images for bundle adjustment processing and orthorectification check.

3.2 Ice Flow Velocity Mapping

16517 ice flow velocity vectors were obtained on ARGON KH-5 and CORONA KH-4A imagery to generate a 240-m-resolution historical ice flow velocity map from 1963 to 1967. Overestimates and underestimates due to acceleration or deceleration of the ice flow were identified and corrected in the ice flow velocity map. The overestimations mainly occurred on the ice sheet, while the underestimations were more prevalent on the ice shelf. The average overestimation was around 35 m/yr, and the average underestimation was approximately 32 m/yr. Since the NG ice shelf is mostly covered by clouds in the ARGON image, the ice flow velocity map was limited to approximately 17 km downstream from the grounding line. The result of the streamflow map is shown in Figure 4a.

The ice flow velocity map has an error of 25 m/yr. This error is expected to cause some underestimation in the ice sheet region due to the uneven and sparse distribution of control points on the ice sheet.

3.3 Ice Flow Velocity Variations

This paper compared the ice flow velocity variations along the center flow lines of NG and ZI from 1963 to 2020, as shown in Figure 4b and Figure 4c. The two glaciers show a significant difference in velocity changes. There was no significant change in ice flow velocity from 1963 to 2005, followed by a noticeable acceleration from 2005 to 2020 for NG. The average ice flow velocity increased by 12.4% from 1963 to 2020 near the grounding line. In contrast, ZI showed slow acceleration in ice flow velocity from 1963 to 2000, followed by rapid acceleration after 2010. Ice flow velocity along the black dashed line in Figure 4c increased by 81.4% from 1963 to 2020.

The spatial variation along the central flow lines for NG showed an acceleration that primarily occurred within the grounding

zone and the interior of the ice sheet, with no significant acceleration observed on the ice shelf beyond the grounding zone. For ZI, a sharp increase in ice flow velocity was observed 20 km upstream from the grounding line, while it began to decelerate gradually downstream from the grounding line.

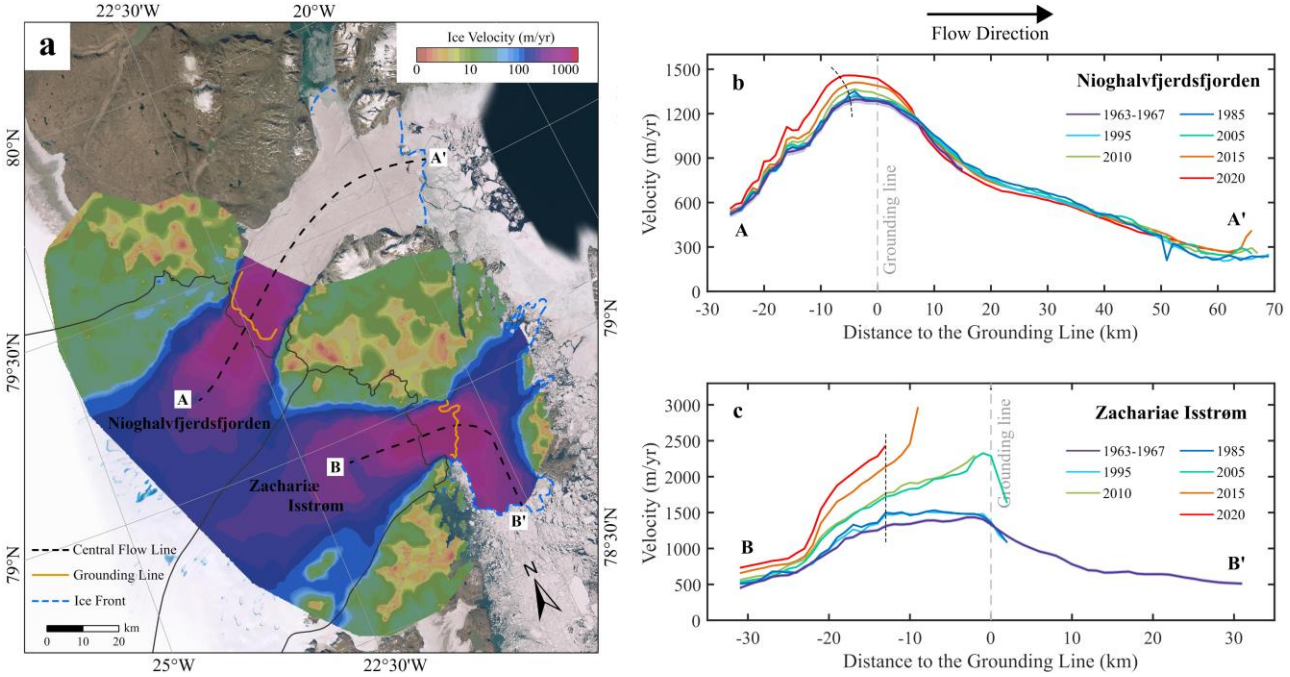

Figure 4. **Historical ice flow velocity in the NG and ZI glacier**. **a** Ice flow velocity map from 1963 to 1967 with the glacier central flow lines marked AA' and BB', respectively. The ice front is taken from 1967 CORONA KH-4A, while the grounding line is 1978 from An and others (2021). Variations in the ice flow velocity of two glaciers along their central flow lines AA' for (**b**) NG and BB' for (**c**) ZI, with the location of grounding lines in grey dash lines. The ice flow velocity uncertainties along the central flow lines are presented by same shaded color as their velocities. The increase rates of ice flow velocity are calculated along the black dash lines.

4. Conclusions and Future Work

The ongoing dynamic changes of NG and ZI in northeastern Greenland have attracted widespread attention. Ice flow velocity is a key parameter for studying glacier changes, and estimating historical ice flow velocity is crucial for predicting future glacier variations. DISP imagery provides a valuable opportunity to study early ice flow motion. However, the distortions present in DISP imagery pose significant challenges for image processing.

In this paper, a practical and systematic orthorectification workflow was successfully applied to CORONA KH-4A imagery, eliminating the panoramic distortions present in eight images and achieving an orthorectification accuracy of 25 m. This provided valuable foundational data for estimating early ice flow velocities. Using the historical velocity reconstruction method proposed by our research group, we successfully created an ice flow velocity map for the NG and ZI glaciers from 1963 to 1967 with an accuracy of 25 m/yr. By combining this data with published ice flow velocity products, we observed different trends along the central flow lines of the two glaciers: NG showed relatively small changes, while ZI experienced significant acceleration.

This paper primarily fills the gap in ice flow velocity data from the 1960s for this region. Future work can use the ice flow velocity data obtained in this study to further estimate the mass balance of the Nioghalvfjerdsfjorden glacier and Zachariae Isstrøm. Additionally, it can investigate the causes of changes in ice flow velocity and assess the stability of these glaciers.

Acknowledgements

This research was supported by the National Natural Science Foundation of China (42394131).

References

An, L., Rignot, E., Wood, M., Willis, J.K., Mouginot, J., Khan, S.A., 2021. Ocean melting of the Zachariae Isstrøm and Nioghalvfjerdsfjorden glaciers, northeast Greenland. *Proc. Natl. Acad. Sci.* 118, e2015483118. doi.org/10.1073/pnas.2015483118.

Choi, Y., Morlighem, M., Rignot, E., Mouginot, J., Wood, M., 2017. Modeling the Response of Nioghalvfjerdsfjorden and Zachariae Isstrøm Glaciers, Greenland, to Ocean Forcing Over the Next Century. *Geophys. Res. Lett.* 44, 11,071-11,079. doi.org/10.1002/2017GL075174.

Feng, T., Li, Y., Wang, K., Qiao, G., Cheng, Y., Yuan, X., Luo, S., Li, R., 2023. A hierarchical network densification approach for reconstruction of historical ice velocity fields in East Antarctica. *J. Glaciol.* 69, 281–300. doi.org/10.1017/jog.2022.58.

Gardner, A.S., Moholdt, G., Scambos, T., Fahnstock, M., Ligtenberg, S., van den Broeke, M., Nilsson, J., 2018. Increased West Antarctic and unchanged East Antarctic ice discharge over the last 7 years. *The Cryosphere*, 12, 521–547. doi.org/10.5194/tc-12-521-2018.

Howat, I.M., Negrete, A., Smith, B.E., 2014. The Greenland Ice Mapping Project (GIMP) land classification and surface elevation data sets. *The Cryosphere*, 8, 1509–1518. doi.org/10.5194/tc-8-1509-2014.

Iacone, B., Allington, G.R.H., Engstrom, R., 2022. A Methodology for Georeferencing and Mosaicking Corona Imagery in Semi-Arid Environments. *Remote Sens.* 14, 5395. doi.org/10.3390/rs14215395.

Joughin, I., 2022. MEaSUREs Greenland Annual Ice Sheet Velocity Mosaics from SAR and Landsat, Version 4. Boulder, Colorado USA. NASA National Snow and Ice Data Center Distributed Active Archive Center. doi.org/10.5067/RS8GFZ848ZU9.

Kim, K., Jezek, K.C., Liu, H., 2007. Orthorectified image mosaic of Antarctica from 1963 Argon satellite photography: image processing and glaciological applications. *Int. J. Remote Sens.* doi.org/10.1080/01431160601105850.

Kim, K.T., 2003. Satellite mapping and automated feature extraction: geographic information system-based change detection of the Antarctic coast. The Ohio State University.

King, M.D., Howat, I.M., Candela, S.G., Noh, M.J., Jeong, S., Noël, B.P.Y., van den Broeke, M.R., Wouters, B., Negrete, A., 2020. Dynamic ice loss from the Greenland Ice Sheet driven by sustained glacier retreat. *Commun. Earth Environ.* 1, 1–7. doi.org/10.1038/s43247-020-0001-2.

Korsgaard, N.J., Nuth, C., Khan, S.A., Kjeldsen, K.K., Bjørk, A.A., Schomacker, A., Kjær, K.H., 2016. Digital elevation model and orthophotographs of Greenland based on aerial photographs from 1978–1987. *Sci.* Data 3, 160032. doi.org/10.1038/sdata.2016.32.

Li, R., Cheng, Y., Cui, H., Xia, M., Yuan, X., Li, Z., Luo, S., Qiao, G., 2022. Overestimation and adjustment of Antarctic ice flow velocity fields reconstructed from historical satellite imagery. *The Cryosphere*, 16, 737–760. doi.org/10.5194/tc-16-737-2022.

Li, R., Ye, W., Qiao, G., Tong, X., Liu, S., Kong, F., Ma, X., 2017. A New Analytical Method for Estimating Antarctic Ice Flow in the 1960s From Historical Optical Satellite Imagery. IEEE Trans. *Geosci. Remote Sens.* 55, 2771–2785. doi.org/10.1109/TGRS.2017.2654484.

Mayer, C., Schaffer, J., Hattermann, T., Floricioiu, D., Krieger, L., Dodd, P.A., Kanzow, T., Licciulli, C., Schannwell, C., 2018. Large ice loss variability at Nioghalvfjerdsfjorden Glacier, Northeast-Greenland. *Nat. Commun.* 9, 2768. doi.org/10.1038/s41467-018-05180-x.

McDonald, R.A., 1995. Corona: success for space reconnaissance, a look into the Cold War, and a revolution in intelligence. *Photgrammetric Engineering & Remote Sensing*, 61(6): 689-720.

Millan, R., Jager, E., Mouginot, J., Wood, M.H., Larsen, S.H., Mathiot, P., Jourdain, N.C., Bjørk, A., 2023. Rapid disintegration and weakening of ice shelves in North Greenland. *Nat. Commun.* 14, 6914. doi.org/10.1038/s41467-023-42198-2.

Moon, T., Joughin, I., Smith, B., Howat, I., 2012. 21st-Century Evolution of Greenland Outlet Glacier Velocities. *Science*, 336, 576–578. doi.org/10.1126/science.1219985.

Mouginot, J., Rignot, E., Scheuchl, B., Fenty, I., Khazendar, A., Morlighem, M., Buzzi, A., Paden, J., 2015. Fast retreat of Zachariæ Isstrøm, northeast Greenland. *Science*, 350, 1357–1361. doi.org/10.1126/science.aac7111.

Olesen, O.B., Reeh, N., 1969. Preliminary report on glacier observations in Nordvestfjord, East Greenland. *Rapp. Grønl. Geol. Unders.* 21, 41–53. doi.org/10.34194/rapggu.v21.7213.

Reeh, N., Thomsen, H.H., Higgins, A.K., Weidick, A., 2001. Sea ice and the stability of north and northeast Greenland floating glaciers. *Ann. Glaciol.* 33, 474–480. doi.org/10.3189/172756401781818554.

Rignot, E., Fenty, I., Menemenlis, D., Xu, Y., 2012. Spreading of warm ocean waters around Greenland as a possible cause for glacier acceleration. *Ann. Glaciol.* 53, 257–266. doi.org/10.3189/2012AoG60A136.

Rosenau, R., Scheinert, M., Dietrich, R., 2015. A processing system to monitor Greenland outlet glacier velocity variations at decadal and seasonal time scales utilizing the Landsat imagery. *Remote Sens. Environ.* 169, 1–19. doi.org/10.1016/j.rse.2015.07.012.

Schaffer, J., Kanzow, T., von Appen, W.J., von Albedyll, L., Arndt, J.E., Roberts, D.H., 2020. Bathymetry constrains ocean heat supply to Greenland’s largest glacier tongue. *Nat. Geosci.* 13, 227–231. doi.org/10.1038/s41561-019-0529-x.

Shin, S.W., 2003. Rigorous Model of Panoramic Cameras. The Ohio State University.

Shin, S., Schenk, T., 2008. Rigorous Modeling of the First Generation of the Reconnaissance Satellite Imagery. *Korean J. Remote Sens.* 24, 223–233.

Sohn, H.G., Kim, G.H., Yom, J.H., 2004. Mathematical modelling of historical reconnaissance CORONA KH-4B Imagery. *Photogramm. Rec.* 19, 51–66. doi.org/10.1046/j.0031-868X.2003.00257.x.

Wallerstein, G., 1958. Movement Observations on the Greenland Ice Sheet. *J. Glaciol.* 3, 207–210. doi.org/10.3189/S0022143000024254.

Ye, W., Qiao, G., Kong, F., Ma, X., Tong, X., Li, R., 2017. Improved Geometric Modeling of 1960s KH-5 ARGON Satellite Images for Regional Antarctica Applications. *Photogramm. Eng. Remote Sens.* 83, 477–491. doi.org/10.14358/PERS.83.7.477.

Zhou, G., Jezek, K., Wright, W., Rand, J., Granger, J., 2002. Orthorectification of 1960s satellite photographs covering Greenland. IEEE Trans. *Geosci. Remote Sens.* 40, 1247–1259. doi.org/10.1109/TGRS.2002.800240.